Topological phase transition in metallic glass formers*

QIN Hairong, HOU Yijie, YANG Kun, JIN Cancan, LYU Yongjun

School of Physics, Beijing Institute of Technology, Beijing 100081, China

Abstract

Metallic glass-forming systems exhibit complex dynamic behaviors during the glass transition. Understanding the dynamic nature of metallic glasses and supercooled liquids is a crucial issue in the study of glassy physics. Topological order provides a novel perspective for re-examining the dynamics of glassy systems and elucidating the physical essence of the glassy state and glass transition. In this study, the microscopic dynamics of CuZr melts in the glass transition are investigated using molecular dynamics simulations. The single-particle dynamic characteristics in the supercooled CuZr melt are the random jump motions of atoms after a long-term caging period. To capture these dynamics, the displacement vector field is constructed based on the spatiotemporal distribution of these jump events. The simulation results reveal that there exist the numerous vortex structures in the displacement vector field. Notably, the vortex formation rate, which is defined as the number of vortices generated per unit time, exhibits a sharp drop near the glass transition temperature. The probability distribution of vortex formation rate displays a bimodal pattern on the drops, indicating the coexistence of two different dynamical states related to vortex formation. Multiple high-strain events are observed surrounding these vortices. It is found that the two vortex states during the transition exhibit markedly different characteristic ratios of vortices to high-strain events (1∶4 *vs* 1∶8), indicating a change in the coupling strength between vortex formation and high-strain activity. The high-strain events predominantly form in the regions between positive and negative vortices, and the specific quantitative relationship between vortices and high-strain events indirectly reflects the presence of strongly interacting vortex-antivortex pairs in the melt. During the vortex state transition, the vortex-to-high-strain-event ratio suddenly doubles, which means that this transition is not only a sudden change in the rate of vortex formation, but also an enhancement of the interactions between vortex-antivortex pairs, representing a change in global topological properties. These

* The paper is an English translated version of the original Chinese paper published in Acta Physica Sinica. Please cite the paper as: QIN Hairong, HOU Yijie, YANG Kun, JIN Cancan, LYU Yongjun，**Topological phase transition in metallic glass formers** . *Acta Phys. Sin.*, 2025, 74(15): 166403. doi: 10.7498/aps.74.20250513

findings demonstrate that the vortex transition exhibits the characteristics of a topological phase transition, thereby predicting the existence of a topological phase transition in the displacement vector field of metallic glass-forming systems. Further speculation suggests that vortices and high-strain events are related to multiple secondary relaxation processes. This study provides a new perspective for understanding the dynamics of glass-forming systems and the glass transition.

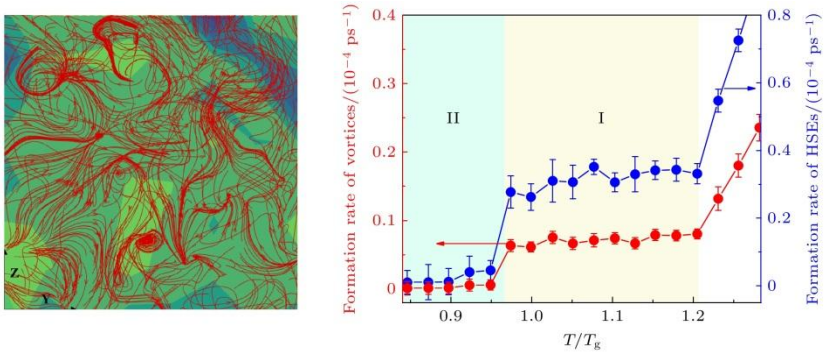

Keywords: topological phase transition; metallic glass; vortex; displacement vector field
PACS: 64.70.-p; 47.32.C-; 64.70.pe; 61.20.Ja
doi: 10.7498/aps.74.20250513
cstr: 32037.14.aps.74.20250513

1. Introduction

One of the most striking features of amorphous materials is the long-range disorder, short-range or local order, of the microscopic atomic arrangement. In recent years, many researchers have devoted themselves to understanding the complex thermodynamic and dynamic properties of amorphous materials, and then to realizing the effective regulation of the properties of amorphous materials. Since AuSi metallic glass was first prepared by Klement et al.[1] in the 1960s, characterizing the microstructure of metallic glasses has been the focus of researchers. Modern microstructure analysis and characterization techniques can well distinguish between amorphous and crystalline, but for different metallic glasses, similar structural information is obtained, which brings a question: why there is a huge difference in the performance of metallic glasses with similar structural information? On the other hand, researchers have proposed a variety of amorphous structure models from theoretical modeling and computer simulation: from the early hard-sphere disordered close-packed model[2] to the atomic cluster model[3,4], Then, at the beginning of the 21st century, Miracle[5] and Sheng et al. [6] respectively proposed similar cluster stacking models. The atomic cluster model gives the local configuration of each atom in the metallic glass[3,4], and statistically classifies the atoms with similar local configurations, which simplifies the seemingly disordered atomic packing into a set containing only hundreds of atomic

clusters. It has further been recognized that some typical cluster motifs in metallic glasses, such as icosahedral clusters and local fivefold symmetry, are closely related to their properties [3,7–11]. However, the cluster-based description also faces several limitations. For example, structural information obtained from cluster analysis does not exhibit a one-to-one correspondence with the properties of amorphous materials, and their correlation varies among different systems. Further studies have revealed that atomic clusters are not randomly arranged but instead exhibit a certain degree of ordering at intermediate length scales, referred to as medium-range order (MRO). Such MRO is believed to be more fundamentally connected to the properties of amorphous materials, including dynamical heterogeneity, relaxation behavior, glass transition, and deformation behavior. Nevertheless, a quantitative characterization of medium-range order remains a major challenge in the structural description of amorphous systems.

Recently, topological concepts have provided a fundamentally new perspective for the structural characterization of amorphous materials. By analyzing extensive radial distribution function data of metallic glasses, researchers have revealed that these systems commonly exhibit crystal-like medium-range translational order, indicating that atomic arrangements in metallic glasses possess a form of topological order at intermediate length scales [12,13]. Wu et al. [14] further demonstrated that the degree of such topological order is closely correlated with the glass-forming ability. The relevance of topology is not limited to metallic glasses. For example, in tetrahedral liquids such as water, simulation studies have shown that the two supercooled liquid states on either side of the liquid–liquid phase transition are characterized by distinctly different topological structures [15]. These findings highlight topology as a powerful tool for understanding amorphous structures. Historically, the importance of topological ideas in physics can be traced back to the 1970s. In their studies of two-dimensional systems, Berezinskii [16], and Kosterlitz and Thouless [17,18] discovered a novel type of phase transition that cannot be described by conventional symmetry-breaking arguments. Instead, this transition is governed by the binding and unbinding of topological defect pairs, namely vortex-antivortex pairs, and is now known as the Berezinskii-Kosterlitz-Thouless (BKT) transition. The BKT transition represents one of the earliest and most influential introductions of topology into physics, greatly broadening our understanding of phase transitions, particularly in low-dimensional systems. Since then, topological concepts have played a crucial role in diverse areas such as the quantum Hall effect, topological insulators, and quantum computation.

Beyond structural characterization, topological defects have also been identified in the dynamical behavior of metallic glasses, where they have been shown to correlate with deformation and relaxation processes. In the deformation of amorphous solids, nonaffine displacement is a key physical quantity for elucidating deformation mechanisms. Previous studies have demonstrated

that, under applied shear stress, the nonaffine displacement fields of elastic amorphous media contain abundant topological defects in the form of vortex-like structures [19,20]. To quantitatively characterize these vortices, Ref. [21] introduced the calculation of Burgers vectors in two-dimensional amorphous displacement fields. It was found that the magnitude of the Burgers vector, corresponding to the vortex density, exhibits a strong correlation with the yielding behavior of the material: a pronounced peak in the number of vortices consistently accompanies each yielding event. Subsequent studies further revealed that vortex interactions and their collective motion play a crucial role in shear-band formation, providing a novel perspective on the plastic deformation of metallic glasses. Wu et al. investigated the normal-mode displacement fields in a two-dimensional amorphous model solid and found that the locations of plastic events coincide with those of negative vortices, which provides a basis for predicting plastic deformation [22]. Topological defects are not confined to amorphous solids. In the translational displacement fields of deeply supercooled metallic-glass-forming melts, a large number of vortex structures have also been observed [23,24]. Near the glass transition, atomic motion in supercooled liquids can be broadly classified into two types: (i) thermal vibrations within local cages defined by nearest neighbors, whose population increases upon cooling; and (ii) intermittent jumping events, in which atoms abruptly relocate after prolonged vibrational motion. Such jumping processes constitute a primary microscopic origin of fast dynamics in deeply supercooled glass-forming liquids. Extensive molecular dynamics simulations have shown that these hopping events are neither isolated nor random. Instead, atoms at neighboring sites tend to hop cooperatively, either simultaneously or sequentially, forming string-like or ring-like patterns that closely resemble the cooperatively rearranging regions proposed in the Adam-Gibbs framework [23]. Our previous molecular dynamics (MD) simulations of CuZr alloys further demonstrated that, when the observation time is extended, the displacement vector field associated with jumping motion develops distinct vortex structures. Notably, the characteristic lifetime of these vortices coincides with the slow β-relaxation time of the system, suggesting that topological defects may provide a microscopic origin for certain complex relaxation processes in metallic glasses [24]. Although topological concepts have begun to offer valuable insights into amorphous systems, their application remains at an early stage. The morphology, evolution, and dynamic roles of topological defects, as well as their connections to various amorphous properties, have yet to be explored in a systematic and comprehensive manner.

Using molecular dynamics simulations, we explore the evolution of topological defects in the translational displacement fields of CuZr alloy melts across the glass formation. Our results suggest the presence of a topological phase transition during glass transition, offering a new perspective on the dynamical mechanisms of the glass transition.

2. Simulation method

2.1 Molecular dynamics simulation

In this paper, the translational dynamics of CuZr alloy during glass transition was studied by classical MD simulation. Firstly, a $Cu_{50}Zr_{50}$ system composed of N = 16384 atoms is prepared. The system was fully relaxed at 1800 K for 2 ns to form an equilibrium liquid phase. The system is then rapidly cooled in an isothermal and isobaric ensemble until the glass transition occurs. The cooling rate was kept at 1×10^{10} K/s, i.e., 2 ns relaxation per 20 K cooling. According to the variation of enthalpy with temperature, the glass transition temperature T_g is approximately 660 K, which is in good agreement with the experimental results[25]. In order to analyze the atomic trajectories, the atomic positions were sampled every 1ps at each temperature for a total sampling time of 48 ns. The interaction between atoms was calculated by using the embedded atom potential of Cu-Zr system developed by Mendelev et al. [26]. In the simulation, the temperature and pressure[27,28] of the system are controlled by the Nóse-Hoover method, the three-dimensional periodic boundary condition is adopted, and the simulation time step is 1fs. The Lammps software package was used for MD simulations [29].

2.2 Displacement vector field analysis

At high temperatures, atoms in the alloy melt predominantly undergo continuous, long-range translational motion. Upon cooling, an increasing fraction of atoms becomes transiently trapped within local cages formed by their nearest neighbors. At certain moments, these atoms escape from the cages and abruptly relocate to new positions, giving rise to jumping events. Such jumping motion gradually becomes the dominant mode of atomic translation during the glass transition. Fig. 1(a) illustrates a representative configuration of an atomic jumping event. The occurrence of jumping can be unambiguously identified from the time evolution of the mean-squared displacement (MSD) of an individual atom. Fig. 1(b) shows the corresponding MSDs for jumping atoms.

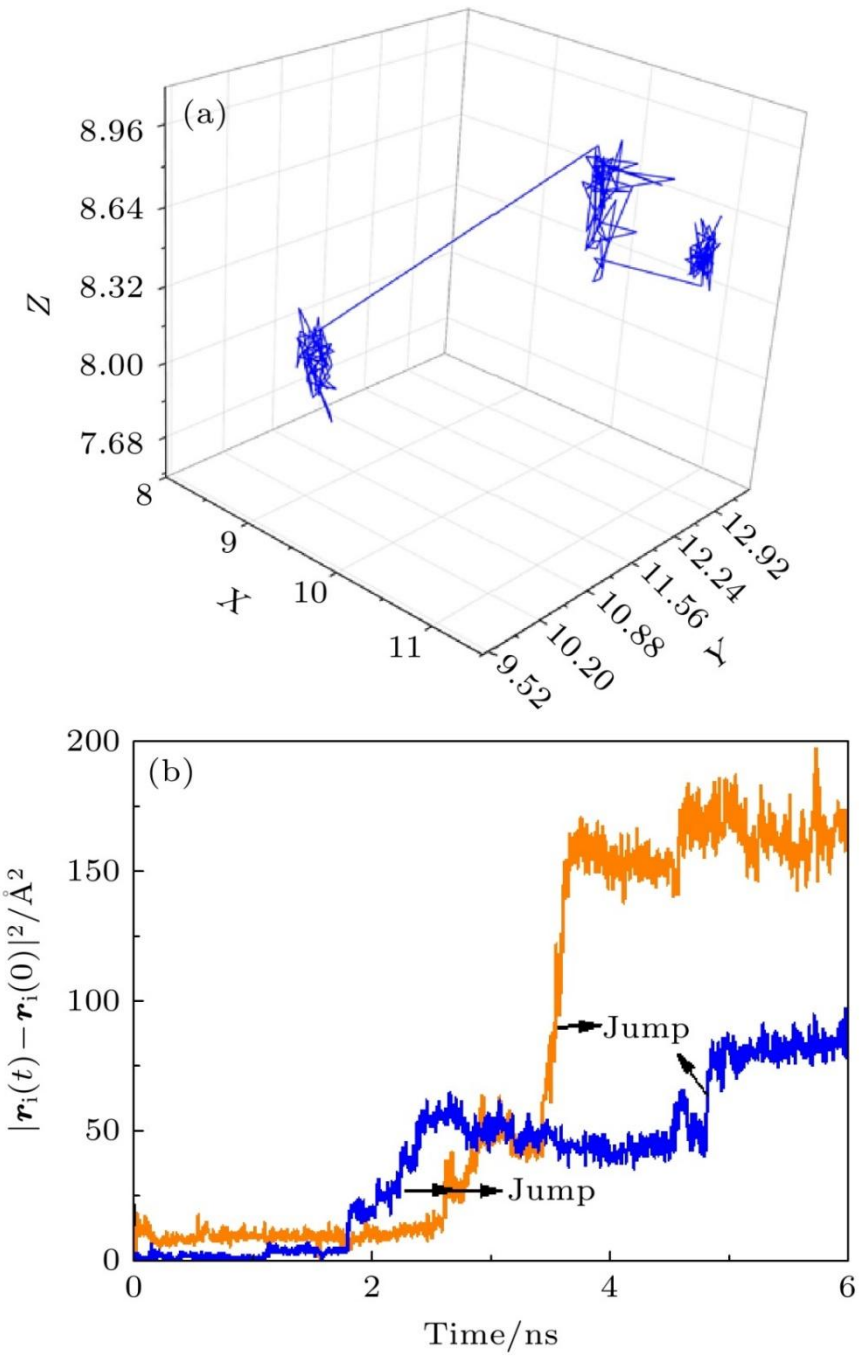

Figure 1. Jumping motion of atoms in CuZr melt: (a) Spatial trajectory of successive jumps; (b) a time-res squared displacement of jumping atoms, orange and blue represent two different types of particles.

In order to accurately judge each jump as well as the jump time and jump distance, we coarse-grain the atomic positions in time, i.e.

$$\overline{\boldsymbol{r}}_i(t) = \frac{1}{\Delta t}\int_0^{\Delta t} \boldsymbol{r}_i(t+t')\mathrm{d}t' , \tag{1}$$

where $\bar{\boldsymbol{r}}_i(t)$ is the coarse-grained position of the atom i at time $t - t + \Delta t$, and Δt is the time window. An atom is identified as undergoing a jumping event when its coarse-grained displacement between two adjacent time windows exceeds three times the Debye-Waller factor. The Debye-Waller factor, which characterizes the mean-squared amplitude of atomic thermal vibrations, is determined at each temperature from MSD. Specifically, the inflection point associated with the caging plateau on the MSD curve is taken as an estimate of the Debye–Waller factor, as illustrated in Fig. 2. In our simulations, a time window of Δt = 200 ps is adopted, in which 41 consecutive atomic configurations are averaged. Tests confirm that this temporal resolution is sufficient to reliably capture individual jumping events. The displacement vector corresponding to each jumping event is $\boldsymbol{j}_i$:

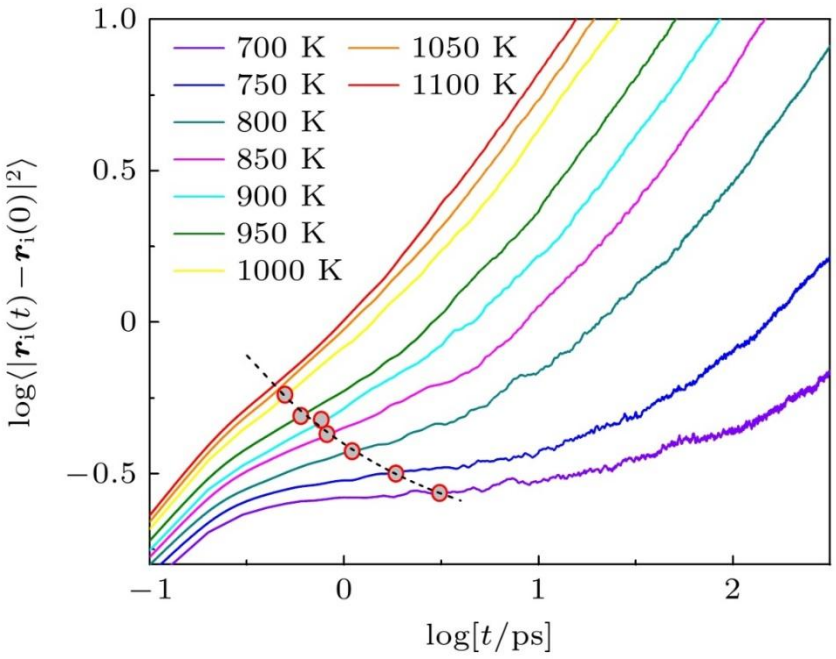

Figure 2. Logarithm plot of mean-squared displacements at various temperatures in CuZr melt, the open circles denote the inflection points in curves and the dashed line is an exponential-function fit to the inflection points.

$$\boldsymbol{j}_i\left(t\right) = \bar{\boldsymbol{r}}_i\left(t+\Delta t\right) - \bar{\boldsymbol{r}}_i\left(t\right), \tag{2}$$

Atoms that are caged by their nearest neighbors throughout the observation interval are assigned a zero displacement vector. In our simulations, different observation times ranging from t_{obs} = 0.4 to 12 ns are examined. For each observation interval, all jumping displacement vectors are recorded, yielding a displacement vector field that captures the spatial form of jumping dynamics. To further simplify the vector field and facilitate the subsequent flow field analysis, the simulation cell is

discretized into $M = 28 \times 28 \times 28$ cubic grids. The jumping displacement vectors within each grid are averaged, resulting in a coarse-grained displacement vector field:

$$\boldsymbol{J}_k = \sum_{t<t_{obs}} \sum_{i \in k} \boldsymbol{j}_i(t) \quad (k = 1, 2, \cdots, M) \tag{3}$$

By calculating the curl of this vector field, the vorticity $\boldsymbol{\omega}$ is obtained:

$$\begin{aligned} \omega_x &= \frac{\partial J_z}{\partial y} - \frac{\partial J_y}{\partial z} \\ \omega_y &= \frac{\partial J_x}{\partial z} - \frac{\partial J_z}{\partial x} \\ \omega_z &= \frac{\partial J_y}{\partial x} - \frac{\partial J_x}{\partial y} \end{aligned} \tag{4}$$

In order to analyze the number and spatial distribution of vortex cores, the Q criterion is used to identify the vortex cores. The parameter Q is defined as

$$Q = \frac{1}{2}\left(\|\boldsymbol{\Omega}\|^2 - \|\boldsymbol{S}\|^2 \right), \tag{5}$$

where $\boldsymbol{\Omega}$ is the vorticity tensor,

$$\Omega_{ij} = 0.5(\partial J_i / \partial r_j - \partial J_j / \partial r_i),$$

$\boldsymbol{S}$ is the strain rate tensor,

$$S_{ij} = 0.5(\partial J_i / \partial r_j + \partial J_j / \partial r_i), (i, j = x, y, z).$$

The Q parameter characterizes the relative magnitude of vorticity and strain. A positive Q indicates that vorticity dominates, signifying the presence of a vortex, whereas a negative Q implies that strain dominates, highlighting regions of pronounced deformation. In this analysis, locations with $Q > 0.1$ are identified as vortices, while regions with $Q < -0.1$ are classified as high-strain events (HSEs).

3. Simulation result

Fig. 3 illustrates representative structural features in the displacement vector field of the supercooled alloy melt at the observation time t_{obs} = 0.4 ns. It can be seen that most hopping events occur cooperatively, forming string- or loop-like patterns in space, as shown in Fig. 3(a). This behavior is consistent with our previous observations [23]. When the observation time is increased to 1.6 ns, distinct vortex structures with different sizes can be clearly identified in the displacement vector field, as illustrated in Fig. 3(b). In our earlier work, we systematically investigated the distribution of vortex numbers at this observation time for different aging times and demonstrated a close connection between vortex statistics and the slow β-relaxation process[24]. The present study further reveals that vortex formation strongly depends on the observation time. As the observation time increases, the number of vortices detected per unit time increases accordingly. When the observation time exceeds approximately 8 ns, the total number of vortices per unit time saturates, indicating the establishment of a steady formation regime. Fig. 3(c) shows a cross-sectional view of the coarse-grained displacement vector field in the *yoz* plane at t_{obs} =12 ns, where well-defined vortex structures are clearly visible. To quantify vortex formation, we define the vortex formation rate as $J = N_V/N_m t_{obs}$, where N_V represents the total number of observed vortex cores, and N_m represents the total number of grids (N_m =M = 28 × 28 × 28), This quantity characterizes the propensity for vortex formation in the system. Fig. 4(a) gives the dependence of the rate of vortex formation and the rate of HSEs on the reduced temperature T/T_g during the glass transition. With decreasing temperature, the vortex formation rate gradually decreases. When the temperature falls below approximately $1.2T_g$, the system enters a temperature-independent plateau regime, where J maintains at about 7.2×10^{-6} ps^{-1} down to about $0.98T_g$. Upon further cooling below $0.98T_g$, J exhibits a sharp drop to approximately 3.2×10^{-7} ps^{-1}, indicating that only a few vortices are formed during the observation time. Notably, the crossover into the plateau regime at $1.2T_g$ occurs smoothly, whereas the transition at $0.98T_g$ is marked by a sudden decrease in J.

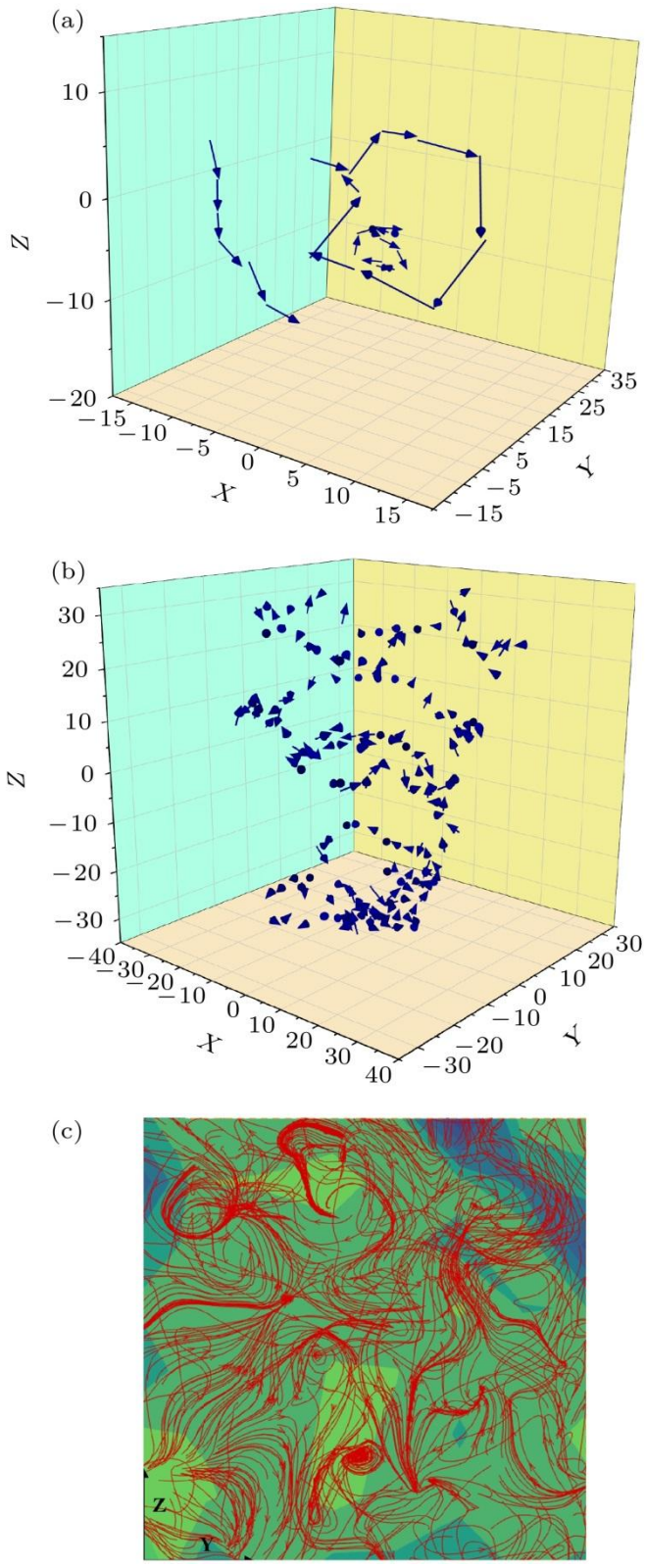

Figure 3. Spatial configuration of jump motions of atoms in supercooled CuZr melt: (a) String- and loop-like configurations observed in a short time interval; (b) vortex that is observed in a relatively long time; (c) a cross section of the flow field of atomic displacements along the *X* direction, which shows a disordered vortex lattice composed of vortices.

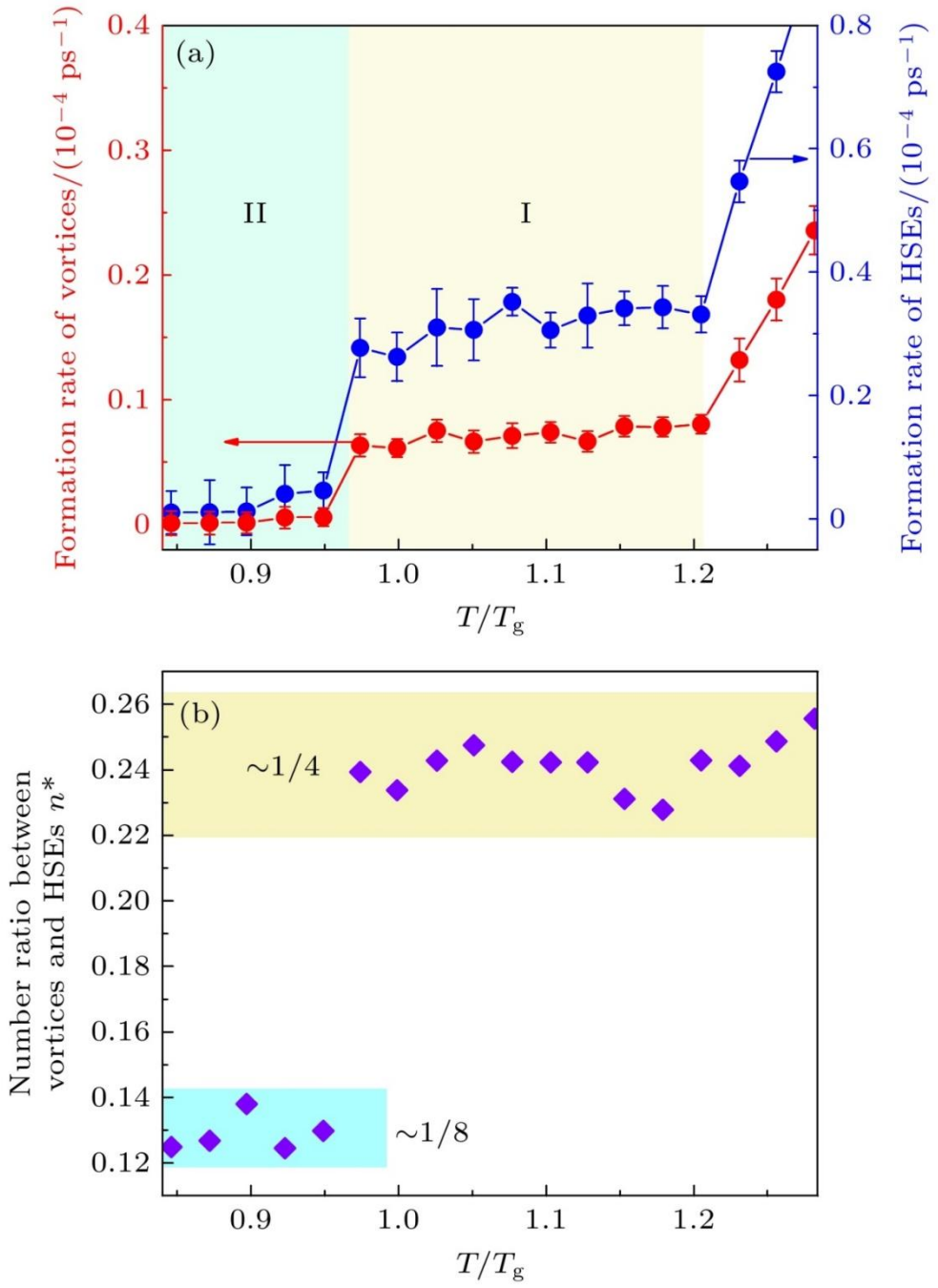

Figure 4. Formation rates of vortices and HSEs: (a) Formation rates of vortices and HSEs versus scaled temperature; (b) ratio of vortex to HSE formation rates as a function of scaled temperature.

To further reveal whether the vortex formation rate at $0.98T_g$ is characterized by a discontinuous transition, 20 independent samples were collected at each temperature, and the probability distribution of the vortex formation rate was analyzed, as shown in the Fig. 5. At high temperatures, the vortex formation rate shows a Gaussian distribution. When the temperature drops to $0.98T_g$, a bimodal distribution appears, and then the distribution returns to a Gaussian form after further cooling. The bimodal distribution clearly shows the coexistence of two vortex states. We denote these two coexisting states as state I in the high-temperature plateau region and

state II in the low-temperature region. A discontinuous transition between these two states occurs in the vicinity of T_g, corresponding to a sudden change in the vortex formation rate, or equivalently, in the number of vortices formed. On the other hand, the radial distribution function and other structural analysis reveal no significant changes in the microscopic structure across T_g. Moreover, thermodynamic quantities of the alloy melt, including density and enthalpy, do not exhibit any discontinuities at T_g. These observations indicate that the vortex-state transition is not accompanied by detectable structural or thermodynamic anomalies. To verify that this transition is not an artifact of computational parameters, the results derived from different observation times t_{obs} = 18, 22 ns were tested first. Although the total number of vortices increase, the vortex formation rate does not change significantly, and the vortex-state transition near T_g persists. Another key parameter is the grid resolution M used to discretize the displacement vector field. Grid discretization is introduced to simplify the vector field and facilitate subsequent flow-field analysis; therefore, M should not be too large, ensuring that the grid spacing exceeds the average nearest-neighbor distance between particles, nor too small, which would risk missing vortex information. Within this criterion, $M = 25 \times 25 \times 25$ and $M = 30 \times 30 \times 30$ were tested, yielding no significant influence on either the vortex formation rate or the vortex-state transition. It can be concluded that the vortex state transition observed in this paper reflects an intrinsic physical property of the system rather than a consequence of computational settings.

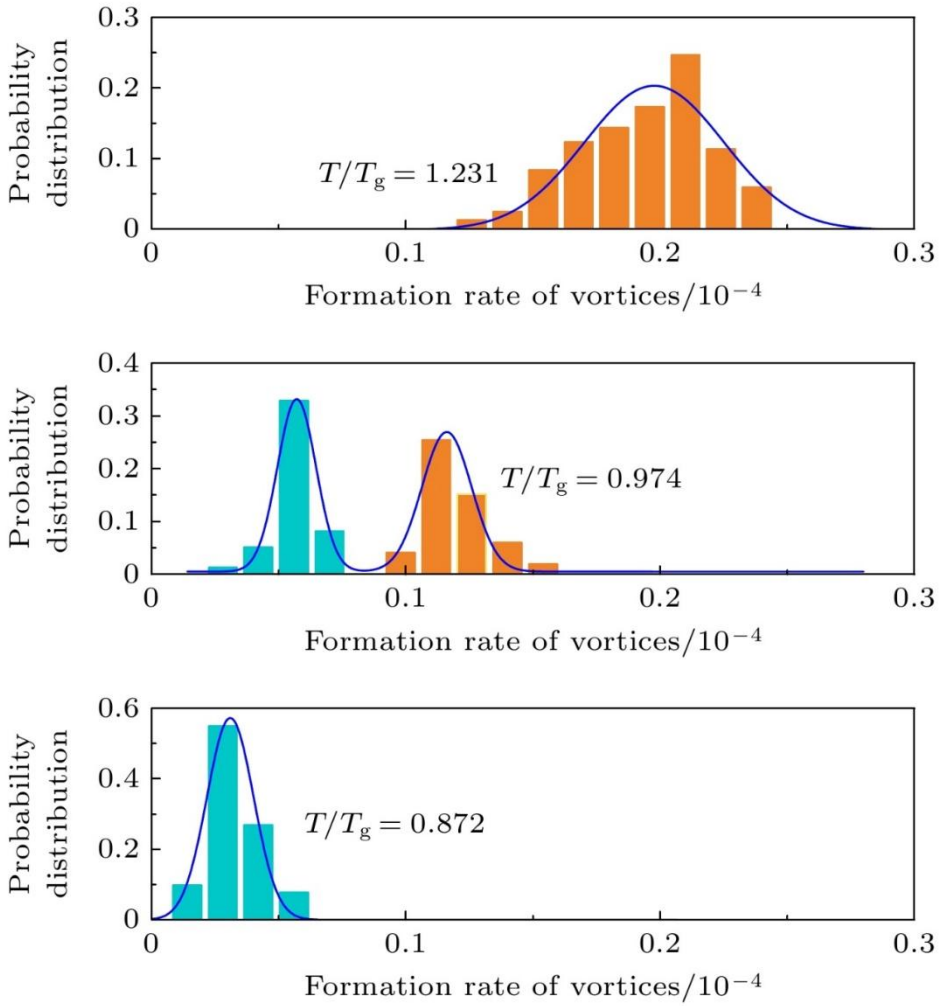

Figure 5. Probability distributions of vortex formation rates at T/T_g = 1.231, 0.974 和 0.872, which spans the vortex transition.

As shown in Fig. 4(a), vortex states I and II exhibit distinct formation rates, i.e., different total numbers of vortices generated per unit time. We further analyzed the HSEs, and found that the number of HSEs is much more than the number of vortices in both the I-state vortex and the II-state vortex phases. Moreover, the occurrence of HSEs is not random but strongly correlated with vortex formation. Specifically, for vortex state I, the ratio of the number of observed vortices to that of HSEs ($n^* = N_V/N_S$, N_V and N_S denote the numbers of vortices and HSEs detected within the observation time t_{obs} time) is approximately 1:4. For vortex state II, this ratio decreases to about 1:8, as shown in Fig. 4(b). Both of them suggest a strong correlation between vortices and HSEs. To elucidate the nature of this correlation, we analyze the spatial configurations formed by vortices and their surrounding HSEs in the two vortex states. Fig. 6(a) presents two representative local structures observed in vortex state I, consisting of a vortex and its four nearest-neighbor HSEs. In the dominant configuration (structure IA), the vortex and its surrounding HSEs are arranged in an approximately planar geometry, as illustrated in the left panel of Fig. 6(a); In another type of arrangement (structure IB), one of the HSEs deviates from the plane, which can be

regarded as a folded or angularly distorted variant of structure IA. Fig. 6(b) shows two typical spatial configurations in vortex state II. Analogous to vortex state I, in structure IIA a single vortex and its eight surrounding HSEs preferentially form a quasi-planar arrangement. The second configuration can be viewed as a folded deformation of structure IIA, in which three HSEs along one edge of the planar structure are displaced out of the plane. Combining the above information, in both vortex states I and II, vortices and their neighboring HSEs organize into well-defined local spatial motifs with a strong tendency toward planar geometries. It should be emphasized that these HSEs are identified within a finite observation window, which means that HSEs may correspond either to a continuous high-strain region surrounding a vortex at a given instant, which is discretized into multiple HSEs, or to a sequence of HSEs occurring at different locations and times near the vortex core. Regardless of these possibilities, the results consistently show that, although the total number of vortices decreases in vortex state II, the number of HSEs associated with each individual vortex approximately doubles. Therefore, the vortex state transition is characterized by a sudden decrease in the vortex-forming ability but a pronounced increase in the incidence of HSEs around a single vortex.

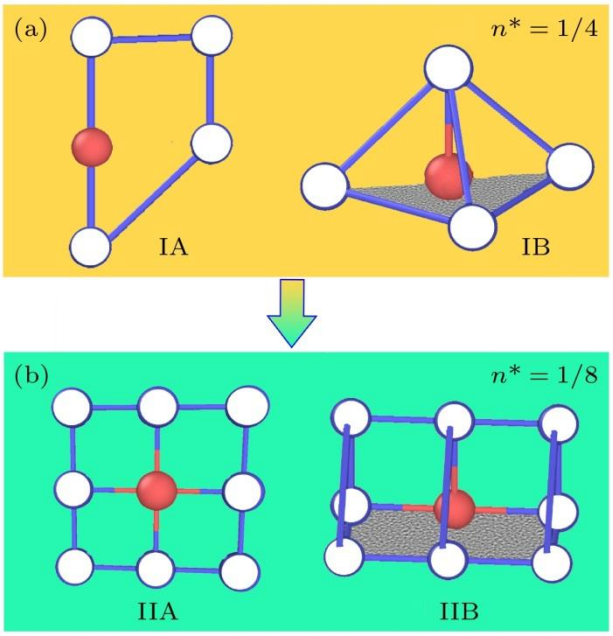

Figure 6. Schematic diagram of vortex and high-strain event pairs. Two configurations of the vortex state I (a) and II (b). The open circles denote the high strain events surrounding a vortex.

4. Discussion

The physical nature of the vortex state transition is our central concern. Since the vortex transition occurs at a temperature close to T_g, and is not accompanied by any discontinuous changes in

thermodynamic quantities such as energy or enthalpy, nor by any pronounced variation in atomic-scale structural features, it does not exhibit the characteristics of a thermodynamic first-order phase transition. In type-II superconductors, magnetic vortex lattices emerge when the applied magnetic field exceeds a critical value. Under external field modulation, these vortex lattices may undergo structural transitions, such as from a hexagonal to a square lattice, or from an ordered lattice to a disordered state. Previous studies have shown that such vortex-lattice transitions are accompanied by latent heat and therefore fall within the framework of Landau phase transitions, which can be theoretically described by the Ginzburg-Landau model [30–32]. These vortex-lattice structural transitions are essentially different from the vortex state transition observed here. The BKT theory of phase transition proposes that at low temperatures two-dimensional superfluids or superconductors host bound pairs of vortices and antivortices. Upon increasing temperature beyond a critical value, these bound pairs dissociate into free vortices. This transition is not associated with symmetry breaking but represents a topological phase transition driven by topological excitations. In the BKT transition, the winding number serves as a topological invariant, and the global topological properties of the system change discontinuously across the transition. In the present three-dimensional system, the direct evaluation of winding numbers is technically challenging. Moreover, vortices and antivortices are not explicitly distinguished in our analysis, preventing a direct identification of bound vortex-antivortex pairs analogous to those in the BKT scenario. Nevertheless, a pronounced coupling between vortices and HSEs is observed. In general, HSEs tend to concentrate in regions between vortices and antivortices. The existence of a well-defined quantitative relationship between the numbers of vortices and HSEs therefore provides indirect evidence for the presence of strongly coupled vortex-antivortex pairs in the melt. Notably, the abrupt doubling of the ratio between the numbers of HSEs and vortices across the vortex-state transition indicates that this transition involves not only a sudden reduction in the vortex formation rate, but also a substantial enhancement of the interactions between vortex-antivortex pairs. Such behavior signifies a change in the global topological properties of the system. In this regard, the transition between vortex states I and II is more consistent with the understanding of the general features of topological phase transitions. The transition between vortex states I and II is a topological phase transition that occurs between two different vortex bound states.

To further clarify the relationship between vortices and HSEs, their autocorrelation functions are calculated,

$$C_X(t) = \langle N_X(0) \cdot N_X(t) \rangle / \langle N_X(0) \cdot N_X(0) \rangle ,$$

where $N_X(0)$ represents the number of vortices or HSEs at time $t = 0$ (subscript X = V for vortices and X = S for HSEs), and $N_X(t)$ represents the number of still remaining vortices or HSEs at time t.

The lifetime of vortex and HSEs can be obtained from the decay time of $C_X(t)$. Fig. 7 shows the autocorrelation function of vortex and HSE with time. It can be seen that the lifetime of vortices is significantly shorter than that of HSEs, and the lifetime of vortices and HSEs after topological transition is significantly longer than that before it. We fit the autocorrelation function to the Kohlrausch-Williams-Watts (KWW) function, $\phi(t) = A\exp\left[-(t/t\tau\tau)^{\gamma}\right]$, where τ is the lifetime of vortex or HSE, and γ is the exponent. However, no single set of KWW parameters can adequately describe the entire decay of either the vortex or HSE autocorrelation function. Instead, the decay of $C_V(t)$ exhibits features of multiple KWW regimes: for $C_V(t)$, the short-time behavior approximately follows the KWW relationship with $\gamma < 1$, and the long-term decay is more consistent with the KWW relationship with $1 < \gamma < 2.5$, indicating an acceleration of vortex decay at longer times; for $C_S(t)$, the behavior in the early stage is similar to that of $C_V(t)$, while an additional secondary decay occurs in the final stage. Due to the strong correlation between vortices and HSEs, they interact dynamically. We believe that the whole process of $C_V(t)$ and the early stage of $C_S(t)$ show similar attenuation characteristics, which is the embodiment of the coupling between vortices and HSEs. At the same time, the high density of HSEs implies significant coupling among HSEs themselves, which can further influence their persistence and may account for the secondary decay observed in $C_S(t)$. The strong correlation between vortices and HSEs also reflects the pronounced coupling between vortices and antivortices, which, in turn, affects the formation, evolution, and lifetime of the high-strain regions between them.

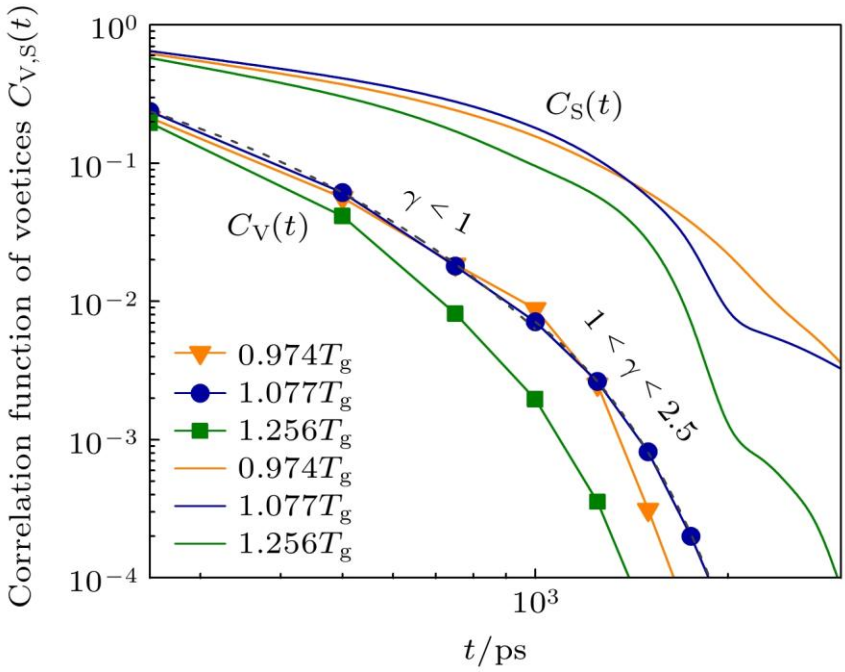

Figure 7. Autocorrelation functions of vortices (symbols) and high strain events (solid lines) at different temperatures. The dashed lines represent the KWW fits with different exponents to the short- and long-time decays of vortices.

In our previous simulation study, it was found that the characteristic timescale associated with vortex formation in the CuZr alloy melt, $\tau_V \propto J^{-1}$, is consistent with the slow β relaxation time of the melt, and the activation energy between them is also very similar. These observations suggest a close connection between vortex formation and the slow β relaxation process [24]. Based on the present results, the fast dynamic region in the system contains vortices and HSEs. Compared with vortices, atoms involved in HSEs exhibit a stronger tendency toward nonlocal and highly mobile dynamics. Furthermore, the emergence of a secondary decay of $C_S(t)$ also implies that there is multiple relaxation associated with HSEs. We speculate that HSEs may be related to fast β relaxation. The quantitative relationship between HSEs and multiple relaxation behavior remains an open issue and constitutes a key objective of our future work. In addition, the observed topological phase transition occurs near the glass transition temperature, and the correlation between the topological transition and the glass transition is also one of the focuses of our subsequent research.

5. Conclusion

MD simulations reveal that vortex structures emerge in the atomic displacement vector field of the CuZr alloy melt during rapid cooling toward the glassy state. It is found that the formation rate of vortex has a discontinuous transition near the glass transition temperature, signaling a transition between two distinct vortex states. Our results further show that a large number of HSEs develop in the vicinity of vortices. There is a characteristic ratio between the formation rate of vortices and HSEs, which indicates that they are closely related, and also implies that there are closely combined vortex and antivortex pairs in the alloy melt. The vortex state transition is accompanied by a doubling of the probability of HSEs around each vortex on average, reflecting a closer interaction between vortices and antivortices. By analyzing the thermodynamic behavior and the topological characteristics associated with the vortex-state transition, we conclude that the observed transition is of topological nature, that is, there is a topological phase transition in the translation vector field of the metallic glass melt. The analysis shows that dynamic vortices and HSEs are related to the multiple secondary relaxation behavior in the system. Future research work will focus on the relationship between this topological phase transition and the glass transition itself, as well as its connection to other dynamical phenomena in amorphous materials, such as kinetic fragility and heterogeneous relaxation dynamics.

References

[1] Klement W, Willens R, Duwez P 1960 *Nature* **187** 869

[2] Bernal J D 1959 *Nature* **183** 141
[3] Cheng Y Q, Ma E 2011 *Prog. Mater. Sci.* **56** 379
[4] Finney J L 1970 *Proc. Roy. Soc. Lond. A* **319** 479
[5] Miracle D B 2004 *Nat. Mater.* **3** 697
[6] Sheng H W, Luo W K, Alamgir F M, Bai J M, Ma E 2006 *Nature* **439** 419
[7] Frank F C 1952 *Proc. R. Soc. Lond. A* **215** 43
[8] Hirata A, Kang L J, Fujita T, Klumov B, Matsue K, Kotani M, Yavari A R, Chen M W 2013 *Science* **341** 376
[9] Li M Z 2017 *Acta Phys. Sin.* **66** 176107
[10] Jiang Y Q, Peng P 2018 *Acta Phys. Sin.* **67** 132101
[11] Wu C, Huang Y J, Shen J 2013 *Chin. Phys. Lett.* **30** 106102
[12] Liu X J, Xu Y, Hui X, Lu Z P, Li F, Chen G L, Lu J, Liu C T 2010 *Phys. Rev. Lett.* **105** 155501
[13] Lü Y J, Entel P 2011 *Phys. Rev. B* **84** 104203
[14] Wu Z W, Li M Z, Wang W H, Liu K X 2015 *Nat. Commun.* **6** 6053
[15] Neophytou A, Chakrabarti D, Sciortino F 2022 *Nat. Phys.* **18** 1248
[16] Berezinskii V L 1971 *Sov. Phys. JETP* **32** 493
[17] Kosterlitz J M, Thouless D J 1973 *J. Phys. C: Solid State Phys.* **6** 1181
[18] Kosterlitz J M 2016 *Rep. Prog. Phys.* **79** 026001
[19] DiDonna B A, Lubensky T C 2005 *Phys. Rev. E* **72** 066619
[20] Del Gado E, Ilg P, Kroeger M, Oettinger H C 2008 *Phys. Rev. Lett.* **101** 095501
[21] Dasgupta R, Hentschel H G E, Procaccia I 2012 *Phys. Rev. Lett.* **109** 255502
[22] Wu Z W, Chen Y, Wang W H, Kob W, Xu L 2023 *Nature Commun.* **14** 2955
[23] Lü Y J, Guo C C, Huang H S, Gao J A, Qin H R, Wang W H 2021 *Acta Mater.* **211** 116873
[24] Lü Y J, Qin H R, Guo C C 2021 *Phys. Rev. B* **104** 224103
[25] Tang M B, Zhao D Q, Pan M X, Wang W H 2004 *Chin. Phys. Lett.* **21** 901
[26] Mendelev M I, Kramer M J, Ott R T, Sordelet D J, Yagodin D, Popel P 2009 *Philos. Mag.* **89** 967
[27] Nosé S 1984 *J. Chem. Phys.* **81** 511
[28] Hoover W G 1985 *Phys. Rev. A* **31** 1695
[29] Plimpton S 1995 *J. Comp. Phys.* **117** 1
[30] Chou C F, Jin A J, Hui S W, Huang C C, Ho J T 1998 *Science* **280** 1424
[31] Mirkovic J, Savel'ev S E, Sugahara E, Kadowaki K 2001 *Phys. Rev. Lett.* **86** 886
[32] Kim S, Hu C R, Andrews M J 2004 *Phys. Rev. B* **69** 094521